# High-pressure-driven multiple-glass transitions of ionic liquids: 1-alkyl-3-methylimidazolium nitrate

Hiroshi Abe [a], [*], Takaaki Hirano [a], Hiroaki Kishimura [a], Takahiro Takekiyo [b], Yukihiro Yoshimura [b]

[a] *Department of Materials Science and Engineering, National Defense Academy, Yokosuka 239-8686, Japan*
[b] *Department of Applied Chemistry, National Defense Academy, Yokosuka 239-8686, Japan*

A B S T R A C T

Ionic liquids, specifically 1-alkyl-3-methylimidazolium nitrate, $[C_n mim][NO_3]$ ($n$ = 4, 6, and 8), underwent pressure-induced amorphization. High-pressure-driven multiple-glass transitions were clarified through Raman spectroscopy. Both double- and triple-glass transitions were observed in $[C_n mim][NO_3]$. Small- and wide-angle X-ray scattering revealed a prepeak representing nanoheterogeneity in $[C_n mim][NO_3]$ ($n$ = 6 and 8) at ambient pressure. Despite the decrease in intensity at glass transition pressure, the prepeak of $[C_8 mim][NO_3]$ still existed. In $[C_8 mim][NO_3]$, the first glass–glass transition occurred a nanoheterogeneous double glass. The second glass–glass transition marked the transition from a heterogeneous to a homogeneous glass.

## 1. Introduction

Water, a simple molecule yet complex liquid, is fundamental to our understanding of molecular structures. The complexity of water becomes evident under high pressures (HPs) as this reveals a complex phase diagram of ice, reflecting the intricate hydrogen bonding network [1]. Researchers have discovered low-density amorphous (LDA) and high-density amorphous (HDA) structures, introducing the concept of water polyamorphism [2–4]. Further studies have led to the concept of "liquid polymorphism," also known as "liquid–liquid transition (LLT)" [5]. The phase diagram predicts that a critical point [4,6] was linking low- and high-density liquids with LDA and HDA, respectively [7,8]. Recent literature summarizes these notable behaviors of water under HP [9].

Ionic liquids (ILs) serve as functional liquid materials [10–12]. The ILs comprising a cation and an anion exhibit nanoheterogeneity. A representative cation is 1-alkyl-3-methylimidazolium ($[C_n mim]^+$), where $n$ indicates the alkyl chain length. Molecular dynamics (MD) simulations [13] have shown that the nanoheterogeneity in the ILs increases with increasing the alkyl chain length. Experimental observations have identified a prepeak on the small- and wide-angle X-ray scattering (SWAXS) patterns, representing the nanoheterogeneity [14]. At low temperature (LT), $[C_n mim][NO_3]$ ($n$ = 6 and 8) amorphized, while other $[C_n mim][NO_3]$ ($n$ = 2, 4, and 10) crystalized [15]. Researchers have determined the LT crystal structures of $[C_n mim][NO_3]$ ($n$ = 2, 4, and 10). $[C_2 mim][NO_3]$ crystallizes simply at LT [16]. In

$[C_4 mim][NO_3]$, crystallization was suppressed upon cooling [17]. Upon heating, cold crystallization was induced and LT crystal polymorph appeared in $[C_4 mim][NO_3]$. The LT crystal polymorph originates from the conformational polymorph of $[C_n mim]^+$ [18]. In $[C_{10} mim][NO_3]$, the phase transition behaviors were extensively influenced by a cooling rate [15]. In addition to the crystal (C) phases, the liquid crystal (LC) phase emerges at LT in $[C_{10} mim][NO_3]$. Upon heating, the C-LC phase transition occurred reversely [15,19]. By using Raman spectroscopy, conformational changes occurred upon phase transition [20]. In the crystal states, four types of $[C_{10} mim]^+$ conformers appeared at LT. The MD simulations demonstrate the liquid (L), LC, and C phases of $[C_n mim][NO_3]$ in the simulation box [21–23]. Each system contains 432 ion pairs in the simulation boxes. The force field parameters [24] were used.

Observations at room temperature revealed HP glasses of $[C_n mim]$ [X] [25–28]. For instance, $[C_n mim][BF_4]$ [27] and $[C_n mim][TFSI]$ [28], where $[TFSI]^-$ is bis(trifluoromethanesulfonyl)imide, occurred glass transitions. In molecular systems, packing polymorphs and conformational polymorphs influence the HP crystal structures [29]. Even in the simple $[C_2 mim][NO_3]$ system, under HP, it induces a complex crystal polymorph [16]. Moreover, multiple pathways of phase transitions emerge under HP. Further, the HP crystal polymorph of $[C_{10} mim][NO_3]$ was determined using SWAXS [19], which is entirely different from the LT one. The complicated LT and HP crystal polymorphs in the ILs are summarized in Table 1.

[*] Corresponding author.
*E-mail address:* ab@nda.ac.jp (H. Abe).

**Table 1**
Classification of layered and non-layered structures of the various ionic liquids.

| Layered (00ℓ Bragg reflections) | | Non-layered (double peak) |
|---|---|---|
| LC-based layered | Hybrid-layered | 3D network |
| LT-[C$_{10}$mim][Cl] | HP-[C$_6$mim][PFBS] | |
| LT-[C$_{10}$mim][Br] | HP-[C$_{10}$mim][Cl] | |
| | LT-[C$_{10}$mim][Br] | HP-[C$_{10}$mim][Br] |
| | LT-[C$_{10}$mim][NO$_3$] | |
| | HP-[C$_{10}$mim][NO$_3$] | HP-[C$_{10}$mim][NO$_3$] |

In this study, we used Raman spectroscopy and SWAXS to examine the HP-driven glass transition of [C$_n$mim][NO$_3$]. We formed a heterogeneous glass in [C$_8$mim][NO$_3$]. Under HP, we induced multiple-glass transitions in [C$_n$mim][NO$_3$].

## 2. Materials and methods

### 2.1. Materials

Herein, we used hydrophilic [C$_n$mim][NO$_3$] (*n* = 6 and 8), purchased from Angene Chemical, Co. We also used another IL, which was [C$_4$mim][NO$_3$] from (IoLiTec GmbH). We vacuum-dried the received samples at room temperature for 48 h using a diaphragm vacuum pump (DTU-20, Ulvac Co.), where the minimum pressure was 200 Pa. The dry diaphragm vacuum pump without oil was required a clean atmosphere that is not contaminated by oil vapor. Moisture analyzer (MS-70, A & D Instruments Co.) was used to estimate the water contents in the ILs after vacuum drying. The water contents of [C$_4$mim][NO$_3$], [C$_6$mim][NO$_3$], and [C$_8$mim][NO$_3$] were found to be 0.93, 0.98, and 0.67 mol% H$_2$O, respectively. We optimized the molecular structures and calculated the wavenumbers of the Raman band using density functional theory (DFT) (Fig. 1).

### 2.2. Raman spectroscopy

We utilized a diamond anvil cell (DAC) for conducing HP Raman spectroscopy. The sample and ruby balls were loaded in the 0.25 mm hole of a pre-indented stainless gasket, which had a thickness of 0.10 mm, within a nitrogen-filled glovebox. To acquire the HP Raman spectra, we employed an NRS-5100 Raman Spectrometer (JASCO Co.) equipped with a monochromator, alongside a Peltier-cooled camera for measurements. Excitation was initiated by a 5.8-mW green laser (wavelength: 532 nm).

### 2.3. SWAXS

We conducted HP SWAXS experiments at ambient temperature using a Mao–Bell-type DAC in the BL-18C of the Photon Factory at KEK [30]. Loading the sample and ruby balls into the hole (diameter: 0.25 mm) of the preindented stainless gasket (thickness: 0.10 mm) within the DAC occurred under a dry-flowing nitrogen atmosphere in a glove bag. Employing double collimators, we obtained a microbeam of diameter 35 μm, and captured 2D diffraction patterns using an imaging plate (IP) system (BAS2500, Fuji-Film Co., Japan) [30]. IP was positioned at a distance of 1273.4 mm for SWAXS. Converting the 2D data into 1D intensity data helped minimize preferred orientation on the Debye rings. To eliminate air scattering, we utilized a vacuum chamber with polyimide (Kapton)-film windows (125-μm thickness). Pressure measurement relied on the spectral shift of the $R_1$ fluorescence line of the ruby balls placed in the sample chamber of the DAC. We calibrated the scattered angles 2θ and the incident wavelength, λ (0.080719 nm) using a standard CeO$_2$ polycrystalline sample.

### 2.4. DFT calculations

DFT optimized the conformations of [C$_8$mim]$^+$ and identified Raman bands assigned to the molecular vibrations. The DFT calculations of [C$_4$mim]$^+$ and [C$_6$mim]$^+$ were calculated in the previous study [18] (Fig. 1). Here, n, t, g, and g' denote *non-planar*, *trans*, *gauche*, and *gauche*', respectively [18]. The energy difference Δ*E* of each conformer was calculated based on the standard of the *non-planar* and all *trans* conformer. All stable conformers of [C$_4$mim]$^+$ are shown in Fig. 1. In [C$_6$mim]$^+$, 13 stable conformers were obtained [18]. Only well-stabilized conformers of [C$_6$mim]$^+$ are represented in Fig. 1. We utilized the B3LYP-D3 including empirical dispersion corrections [31] and hybrid functional and 6–311 + + G(d,p) basis set of *GAMESS* for all DFT calculations [32]. Three conformers of [C$_8$mim]$^+$ were calculated previously using the DFT calculations [33]. Referring the well-stabilized conformers of [C$_6$mim]$^+$, the initial conformations of [C$_8$mim]$^+$ in the DFT calculations were selected.



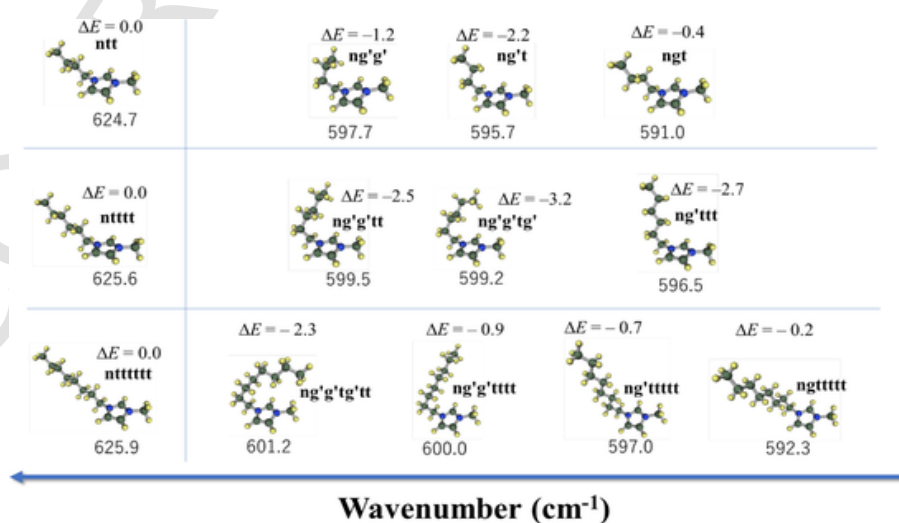| ΔE = 0.0 ntt 624.7 | ΔE = −1.2 ng'g' 597.7 | ΔE = −2.2 ng't 595.7 | ΔE = −0.4 ngt 591.0 | |
|---|---|---|---|---|
| ΔE = 0.0 ntttt 625.6 | ΔE = −2.5 ng'g'tt 599.5 | ΔE = −3.2 ng'g'tg' 599.2 | ΔE = −2.7 ng'ttt 596.5 | |
| ΔE = 0.0 nttttt 625.9 | ΔE = −2.3 ng'g'tg'tt 601.2 | ΔE = −0.9 ng'g'tttt 600.0 | ΔE = −0.7 ng'tttt 597.0 | ΔE = −0.2 ngtttt 592.3 |

**Wavenumber (cm⁻¹)**

**Fig. 1.** Molecular structures of [C$_n$mim]$^+$ (n = 4, 6, and 8). Conformations were optimized, and the wavenumbers of the Raman bands (cm$^{-1}$) were calculated using the DFT calculations. The numbers in the figure reveal the energy difference, ΔE (in kJmol$^{-1}$), of each conformer from the non-planar and all trans conformer. ΔE of [C$_4$mim]$^+$ and [C$_6$mim]$^+$ was obtained in the previous study [18].

## 3. Results and discussion

### 3.1. High-pressure glass on [$C_n$mim][$NO_3$] (n = 4, 6, and 8)

The method for determining the glass transition pressure ($P_g$) was proposed through the line-broadening of ruby $R_1$ fluorescence [34]. Initially, $P_g$ upon compression was determined for [$C_2$mim][$BF_4$] [25]. Specifically, the full width at half-maximum (FWHM) of the ruby $R_1$ fluorescence line exhibited a sudden increase at $P_g$. In addition, the pressure dependence of the difference in FWHM ($\Delta$FWHM) between FWHM at HP and FWHM$_0$ at ambient pressure was revealed the multiple-glass transitions of the ILs [27,28].

Fig. 2(a)–2(c) illustrate the pressure dependencies of $\Delta$FWHM in [$C_n$mim][$NO_3$] (n = 4, 6, and 8) at room temperature, respectively. Using a few ruby balls inside the DAC, the observed FWHM and pressure were averaged. $\Delta$FWHM was calculated by subtracting of FWHM$_0$. Upon compression, $\Delta$FWHM increased drastically at approximately 2.5 GPa ($P_g$), leading to the amorphization of [$C_4$mim][$NO_3$] (Fig. 2(a)). Crystallization was suppressed in [$C_4$mim][$NO_3$], upon compression. Although $\Delta$FWHM slightly decreased above 4.8 GPa, line-broadening occurred above 6.5 GPa ($P_1$) with increasing pressure (Fig. 2(a)). Similar to the multiple-glass transition observed in [$C_4$mim][$BF_4$] [27] exhibited a double-glass transition of [$C_4$mim][$NO_3$] under HP. To examine effect of alkyl chain length on multiple-glass transitions, we measured pressure-dependent line-broadening in [$C_6$mim][$NO_3$]. Fig. 2(b) shows the pressure dependence of $\Delta$FWHM in [$C_6$mim][$NO_3$]. The increase in $\Delta$FWHM at 2.7 GPa ($P_g$) indicates the glass transition of [$C_6$mim][$NO_3$]. $P_g$ of [$C_6$mim][$NO_3$] was comparable to that of [$C_4$mim][$NO_3$]. Upon further compression, the first glass–glass transi-

tion of [$C_6$mim][$NO_3$] was observed at approximately 6.7 GPa ($P_1$). Both [$C_4$mim][$NO_3$] and [$C_6$mim][$NO_3$] exhibit a double-glass transition when considering their pressure behaviors. In a previous study [27], [$C_6$mim][$BF_4$] demonstrated a triple-glass transition under HP, thereby clarifying the anion effect for multiple-glass transitions in the [$C_6$mim][X] system. Fig. 2(c) illustrates an entirely different HP behavior observed in [$C_8$mim][$NO_3$]. [$C_8$mim][$NO_3$] underwent amorphization at lower pressure ($P_g$ = 1.8 GPa). Additionally, $P_1$ (5.7 GPa) of [$C_8$mim][$NO_3$] was smaller than those of [$C_4$mim][$NO_3$] and [$C_6$mim][$NO_3$]. Moreover, the second glass–glass transition occurred at $P_2$ (7.1 GPa) only in [$C_8$mim][$NO_3$]. Subsequently, complicated glassy states emerged in [$C_8$mim][$NO_3$], resulting in changes in the local disorders.

Fig. 3(a)–3(c) plot the glass transition pressures of [$C_n$mim][X] to emphasize the anion effect of the glass transitions as an inherent HP property. For a comparison, the previously obtained glass transition pressures of [$C_n$mim][TFSI] [28] and [$C_n$mim][$BF_4$] [27] are shown in Fig. 3(a) and (c), respectively. The interaction energy between [$C_4$mim]$^+$ and anions was estimated previously [35,36]. For instance, the interaction energy increases in the order of [TFSI]$^-$ < [PF$_6$]$^-$ < [BF$_4$]$^-$ < [ClO$_4$]$^-$ < [SCN]$^-$ < [I]$^-$ < [NO$_3$]$^-$ < [Br]$^-$ < [OAc]$^-$, and



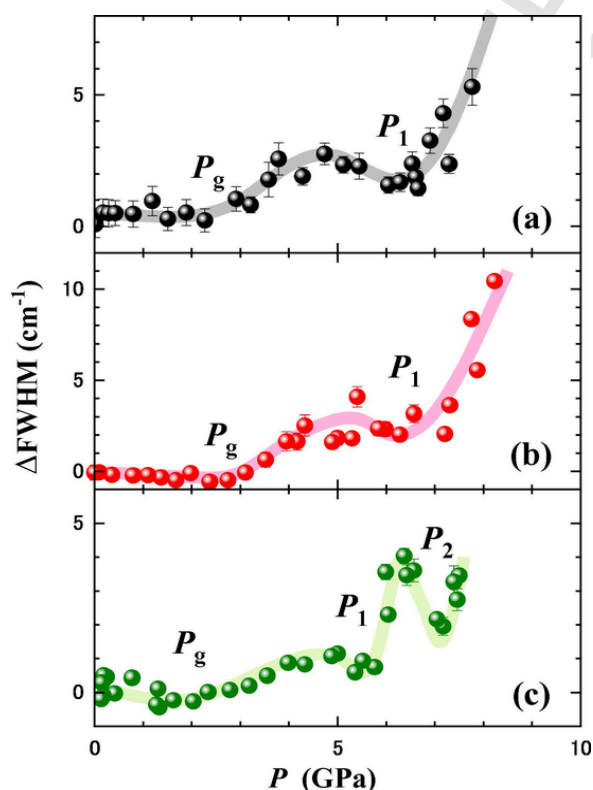**Fig. 2.** Difference in full width at half-maximum ($\Delta$FWHM) for ruby $R_1$ fluorescence line as a function of pressure in (a) [$C_4$mim][$NO_3$], (b) [$C_6$mim][$NO_3$], and (c) [$C_8$mim][$NO_3$]. Lines serve as visual guides. $P_g$, $P_1$, and $P_2$ denote the glass transition pressure, the first glass–glass transition pressure, and the second glass–glass transition pressure, respectively.
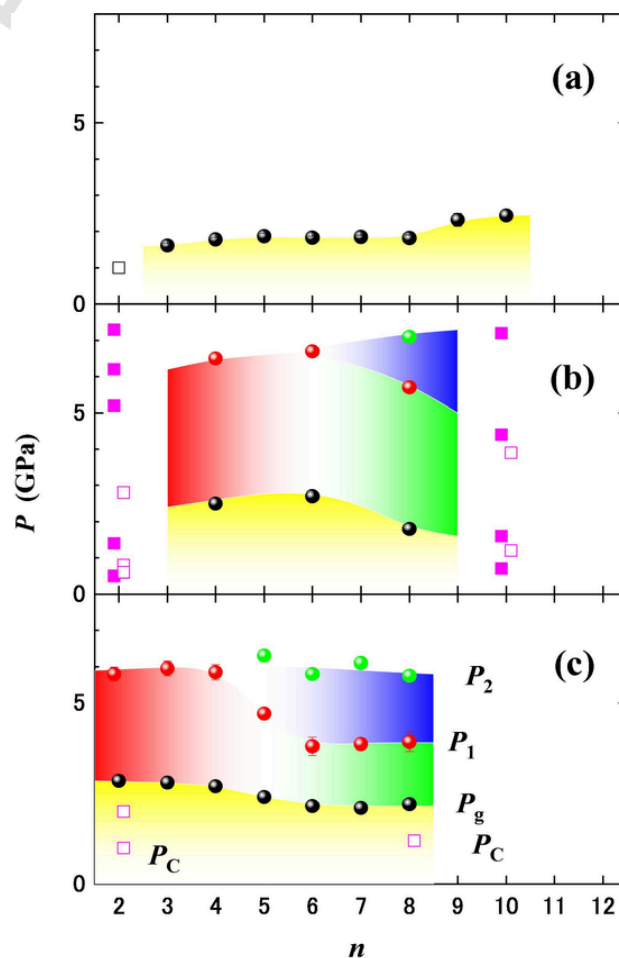


**Fig. 3.** Crystallization and glass transition pressures in (a) [$C_n$mim][TFSI], (b) [$C_n$mim][$NO_3$], and (c) [$C_n$mim][$BF_4$]. $P_C$, $P_g$, $P_1$, and $P_2$ denote the crystallization pressure, the glass transition pressure, first glass–glass transition pressure, and second glass–glass transition pressure, respectively. The circles reveal the glass transition pressures. The closed and open squares reveal crystal-crystal phase transitions upon compression and decompression, respectively.

[Cl]⁻ < [F]⁻. Here, [TFSI]⁻ is categorized as a weak interaction. The molecular shape of [TFSI]⁻ is anisotropic, and [TFSI]⁻ possesses a dipole moment [37]. Further, [TFSI]⁻ possesses two stable conformers (*cis* and *trans*) [37]. $[C_nmim][TFSI]$ was characterized by prepeaks, which represent the nanoheterogeneity [38]. Fig. 3(a) exhibits the HP-driven glass transition of $[C_nmim][TFSI]$ [27]. A single glass transition appeared in $[C_nmim][TFSI]$ ($3 \le n \le 10$). The $P_g$ values of $[C_9mim]$ [TFSI] and $[C_{10}mim][TFSI]$ increased slightly due to nanoheterogeneity as it developed with increasing alkyl chain length. The random freezing of anionic *cis* and *trans* conformers was considered as a glass-forming factor in $[C_nmim][TFSI]$. We deduced that random freezing of the *cis* and *trans* conformers of [TFSI]⁻, which causes the HP-amorphization. The prepeak in $[C_{10}mim][TFSI]$ [38] did not vanish above $P_g$; therefore, super-pressurized liquid (spL) was amorphized to exhibit nanoheterogeneity. Meanwhile, $[C_2mim][TFSI]$ simply crystallized at approximately 1 GPa [39]. In contrast to anisotropic [TFSI]⁻, $[PF_6]^-$ has no conformational degrees of freedom. Due to the weak interaction energy of $[PF_6]^-$ [34], $[C_nmim][PF_6]$ ($n$ = 6 and 8) indicated glass transition under HP [26]. In the $[C_nmim][NO_3]$ system, $[NO_3]^-$ belongs to the medium interaction energy group [35]. $[C_2mim][NO_3]$ presented the HP crystal polymorph and multiple pathways of phase transition [16]. Additionally, we observed a reversible crystal polymorph of $[C_{10}mim][NO_3]$ under HP [19]. The glass transition pressures including the crystal phases are plotted in Fig. 3(b). In spite of the medium interaction energy of $[NO_3]^-$, HP-driven multiple-glass transitions were induced in $[C_nmim][NO_3]$ ($n$ = 4, 6, and 8). In particular, the triple-glass transition of $[C_8mim][NO_3]$ appeared upon compression. $[BF_4]^-$ is characterized as the weak interaction energy [35]. HP behaviors in $[C_nmim][BF_4]$ as another IL system are indicated on the alkyl chain length scale (Fig. 3(c)). Upon compression, HP glass appeared in $[C_2mim][BF_4]$ [25]. In contrast, the crystal polymorph of $[C_2mim][BF_4]$ occurred upon decompression. Also, decompression-induced crystallization was observed in $[C_8mim][BF_4]$ [27]. Mean-

while, HP-driven multiple-glass transitions were detected upon compression. The multiple-glass transitions occurred without crystallization in the intermediate alkyl chain length ($n$ = 3–7), (Fig. 3(c)). Even in $[C_5mim][BF_4]$, the triple-glass transition was due to under HP. Moreover, the prepeak of $[C_8mim][BF_4]$ disappears at $P_g$. $[C_8mim][BF_4]$ exhibits a homogeneous glass, contrasting with the nanoheterogeneous glass of $[C_{10}mim][TFSI]$. The alkyl chain length region of the triple-glass transition of $[C_nmim][BF_4]$ is enlarged compared with that of $[C_nmim][NO_3]$.

### 3.2. Conformational changes in $[C_nmim][NO_3]$ under high pressure

Raman spectroscopy determined the complicated crystal polymorph of $[C_{10}mim][NO_3]$ at LT [20]. When crystallization occurred at LT, the broad Raman bands in the liquid state transformed into sharp Raman bands, allowing the distinction between ordered and disordered states based on the bandwidth.

Fig. 4(a) shows the pressure dependence of $[C_4mim]^+$ conformers. We utilized the asymmetric profile fitting to decompose the observed Raman bands employing the asymmetric pseudo-Voigt function. The stable conformers (ntt, ngt, ng't, and ng'g') of $[C_4mim]^+$ were calculated using DFT (Fig. 1) [18]. Here, n, t, g, and g' denote *non-planar*, *trans*, *gauche*, and *gauche'*, respectively [18]. In a previous study of fluorinated ILs [40], sharp Raman bands of $[C_4mim]^+$ (ntt, ngt, ng't, and ng'g') were observed alongside accompanying the LT crystallization. For $[C_4mim][NO_3]$, Raman bands of the *trans* and *gauche* conformers of $[C_4mim]^+$ in the liquid state appeared at 580–630 cm⁻¹ (Fig. 4(a)). The Raman spectra at the above wavenumber region originated from the $CH_2$ rocking mode of $[C_4mim]^+$. The *gauche* band of $[C_4mim]^+$ at ambient pressure was broader than the *trans* band. One of the reasons is that the broad *gauche* band contains the ngt, ng't, and ng'g' conformers [40], whose wavenumbers are different (Fig. 1). Peak sharpening was not observed up to the maximum pressure. This means that HP crystal-
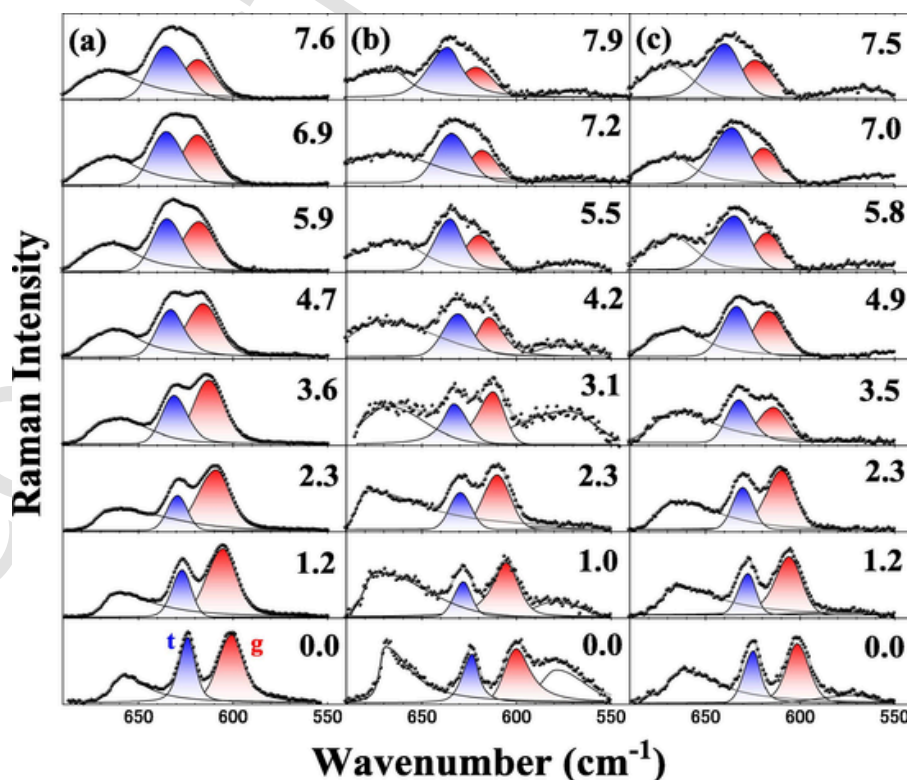


**Fig. 4.** Raman spectra at room temperature of (a) $[C_4mim][NO_3]$, (b) $[C_6mim][NO_3]$, and (c) $[C_8mim][NO_3]$. Cationic Raman bands are observed at 580–630 cm⁻¹. The numbers in the figure indicate the pressure values (GPa).

lization was suppressed in [C$_4$mim][NO$_3$] upon compression. The Raman intensities varied with pressure. For instance, above 5.9 GPa, the *trans* band intensity became larger than the *gauche* intensity. Fig. 4(b) presents the pressure-dependent Raman spectra of [C$_6$mim][NO$_3$]. The stable conformers of [C$_6$mim]$^+$ that were calculated using the DFT [18], are represented in Fig. 1. In the same manner at ambient pressure with [C$_4$mim]$^+$, the *trans* conformer (nttttt) of [C$_6$mim]$^+$ was shaper than the *gauche* conformers (ng'g'tt, ng'g'tg', and ng'ttt). Additionally, with increasing pressure, peak broadening of the *trans* conformer was observed in [C$_6$mim][NO$_3$]. The Raman intensity of the *trans* conformer exceeded the *gauche* one and the long alkyl chain effect under HP was examined in [C$_8$mim][NO$_3$]. The stable [C$_8$mim]$^+$ conformers were estimated using DFT in this study, referring to the conformers of [C$_6$mim]$^+$ (Fig. 1). The ntttttt conformer of [C$_8$mim]$^+$ belongs to the *trans* group. The other ngtttttt, ng'ttttt, ng'g'tttt, and ng'g'tg'tt conformers are classified into the *gauche* group. We express the HP tendency of the [C$_8$mim]$^+$ conformers by the *trans* dominant pressure region above 3.5 GPa. Compared with [C$_4$mim]$^+$ and [C$_6$mim]$^+$, the *trans* [C$_8$mim]$^+$ was preferred as a major conformation in the lower pressure region, which means that *trans* conformers such as [C$_8$mim]$^+$ could be favorable for longer alkyl chain packing under densely packed conditions.

Quantitative conformational analysis is important for detailed molecular behaviors, which relate to the HP-driven multiple-glass transition. Fig. 5(a)–5(c) show the conformational ratios of [C$_4$mim][NO$_3$], [C$_6$mim][NO$_3$], and [C$_8$mim][NO$_3$], respectively. The pressure dependence of intensity fractions, $f_i$, were obtained from profile fitting. $f_i$ of the [C$_n$mim]$^+$ conformers is provided by,

$$f_i = \frac{I_i}{I_t + I_g} \tag{1}$$

where $I_t$ and $I_g$ are the Raman intensities of the *trans* and *gauche* conformers, respectively. The conformations of [C$_4$mim][NO$_3$] drastically changed upon compression, which is related to the glass transitions (Fig. 5(a)). At $P < P_g$ in the spL state, the *gauche* conformers (ng'g', ng't, and ngt) of [C$_4$mim]$^+$ increased gradually as pressure increases The ntt conformer changed to a folding conformer during spL. In contrast, above $P_g$, conformational fraction of the *gauche* conformers (ng'g', ng't, and ngt) in the glassy state decreased proportionally with pressure. The *trans* alkyl chains for a higher packing efficiency could be promoted for further packing in the glassy state. Approximately at around $P_1$, a major conformer was exchanged with the *trans* conformer of [C$_4$mim]$^+$. The first glass–glass transition at $P_1$ was caused by conformational switching.

Fig. 5(b) plots the pressure properties of [C$_6$mim]$^+$, in which the *gauche* conformers (ng'g'tt, ng'g'tg', and ng'ttt) in the spL was mainly occupied. Nevertheless, at approximately $P_g$, *trans* [C$_6$mim]$^+$ became the major conformer instead of the *gauche* conformer. The *trans* conformer contributed to the higher molecular packing efficiency in the glass state. At $P_1$, a discontinuous increase in the *trans* fraction was observed. We explained the double-glass transition of [C$_6$mim][NO$_3$] through the conformational changes of [C$_6$mim]$^+$.

[C$_8$mim][NO$_3$] provided the pressure-sensitive conformations of [C$_8$mim]$^+$ (Fig. 5(c)). A relatively large portion at ambient pressure of the *gauche* conformers (ng'g'tg'tt, ng'g'tttt, ng'ttttt, and ngtttttt) was observed. By pressing the sample, the *gauche* conformers such as ng'g'tg'tt, ng'g'tttt, ng'ttttt, and ngtttttt increased during spL. Once the pressure reached $P_g$, the *gauche* fraction decreased inversely. The rapid conformational changes of [C$_8$mim]$^+$ above $P_g$ could modify the local arrangement for dense packing. The conformational crossover pressure from the *gauche*-dominant conformers (ng'g'tg'tt, ng'g'tttt, ng'ttttt, and ngtttttt) to the *trans*-dominant conformers was 3 GPa. Without the glass–glass transition ($P_g < P < P_1$), the rapid increment of the *trans* [C$_8$mim]$^+$ conformer could be caused by densely molecular packing (Fig. 1). The [C$_8$mim]$^+$-inherent *trans* conformers enable us the enlargement of the *trans* fraction ($f_t = 0.65$). However, in the first glass–glass transition at $P_1$, a conformational change was not observed (Fig. 5(c)). We characterized the new glassy state by pressure-invariant conformational fractions at $P_1 < P < P_2$. Notably, the second glass–glass transition at $P_2$ was influenced by the conformational changes. Above $P_2$, the *gauche* conformers (ng'g'tg'tt, ng'g'tttt, ng'ttttt, and ngtttttt) of [C$_8$mim]$^+$ increased again. The HP glassy states in [C$_8$mim][NO$_3$] are classified into pressure-variant and pressure-invariant conformations.

### 3.3. Pressure dependence of nanoheterogeneity in [C$_n$mim][NO$_3$]

The nanoheterogeneities of [C$_n$mim][NO$_3$] ($n = 4$, 6, and 8) were investigated using SWAXS. The SWAXS patterns at ambient pressure are shown in Fig. 6. We normalized the SWAXS intensities by the scattering intensity of the Kapton film. Obviously, the prepeak intensity of [C$_8$mim][NO$_3$] was large, and the prepeak was located at the low-$Q$ position, which indicates the correlation length (2.3 nm) between the nonpolar nanodomains. For instance, the MD simulation of [C$_{10}$mim][TFSI] presents that the 2-nm$^{-1}$ prepeak is derived from the ion – ion distances mediated by nonpolar nanodomains [38]. The MD simulation of [C$_8$mim][NO$_3$] provided a 2.26-nm stacking sequence of the crystal phase [21]. Moreover, a snapshot in the liquid state supported a correlation length of 2.3 nm. Thus, the local structure of [C$_8$mim][NO$_3$] in the liquid state at ambient pressure could be represented by a partial-LC-like stacking structure. Further, a broad and weak prepeak was observed in [C$_6$mim][NO$_3$] (Fig. 6). The distribution of the correlation
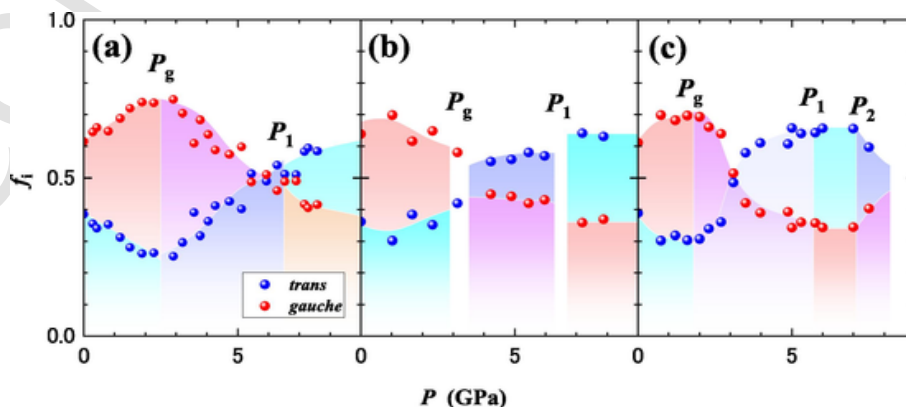


**Fig. 5.** Pressure dependences of intensity fractions, $f_i$, in (a) [C$_4$mim][NO$_3$], (b) [C$_6$mim][NO$_3$], and (c) [C$_8$mim][NO$_3$]. $P_g$, $P_1$, and $P_2$ denote the glass transition pressure, the first glass–glass transition pressure, and the second glass–glass transition pressure, respectively.
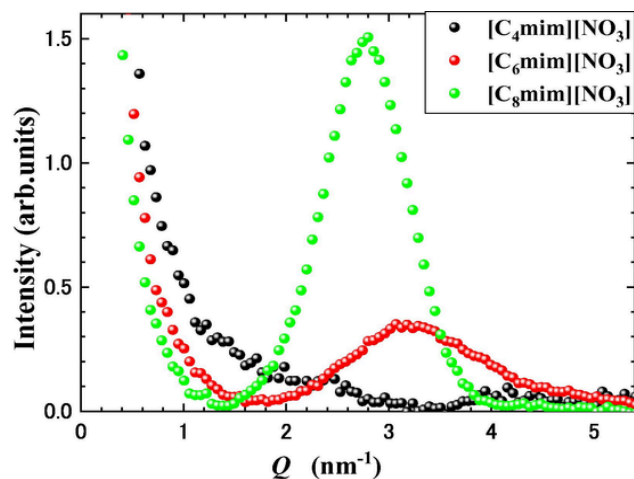
**Fig. 6.** Pressure dependence of the SWAXS patterns of $[C_n mim][NO_3]$ ($n = 4, 6$, and 8) at room temperature and ambient pressure.

length reflected the prepeak width. The broad prepeak at ambient pressure was originated from various conformers and the orientational disorder of $[C_6 mim]^+$. The 3.2-$nm^{-1}$ prepeak corresponds to a shorter correlation length of 2.0 nm. In case of $[C_4 mim][NO_3]$, there was no prepeak at ambient pressure. Therefore, the homogeneous spL in $[C_4 mim][NO_3]$ transformed into homogeneous glass under HP. The nanoheterogeneity of $[C_n mim][NO_3]$ was found to develop proportionally to the alkyl chain length at ambient pressure.

Fig. 7(a) presents the pressure-dependent SWAXS patterns of $[C_6 mim][NO_3]$. By pressing, the SWAXS intensity decreased immediately and the prepeak almost vanished at 0.5 GPa ($<P_g$). Further, the nanoheterogeneity of $[C_6 mim][NO_3]$ in the spL state collapsed easily, and the nanoheterogeneity was flexible. At $P_g$, the homogeneous glass was completely formed in $[C_6 mim][NO_3]$ due to no prepeak. Entirely different HP SWAXS patterns were obtained in $[C_8 mim][NO_3]$ (Fig. 7(b)). The prepeak intensity gradually decreased up to 1.1 GPa ($<P_g$) without changing the prepeak width. Some parts below 1.1 GPa of the nanoheterogeneity changed to the homogeneous part with decreasing prepeak intensity. Homogeneous and nanoheterogeneous parts coexisted in the spL state of $[C_8 mim][NO_3]$. Notably, at 2.0 GPa ($>P_g$), the prepeak did not vanish completely but the prepeak broadening occurred distinctly (Fig. 7(b)). At $P_g$, some parts of the nanoheterogeneity remained even in the glass transition. Thus, the nanoheterogeneity of $[C_8 mim][NO_3]$ was found to be relatively rigid compared with $[C_6 mim][NO_3]$. A new finding is that the glass transition of $[C_8 mim][NO_3]$ in the spL caused a change in the nanoheterogeneous morphology due to prepeak broadening at $P_g$. Inside the homogeneous part of the $[C_8 mim][NO_3]$ glass, various kinds of nanodomains, which obey the wide distribution of the correlation lengths, exist, compensating for their size mismatches. By further compression, the line profile of the prepeak changed at 5.0 GPa. The peak shape was represented by a superposition of two prepeaks. Hence, two components of the nanoheterogeneities were expressed by correlation lengths of 1.68 and 2.24 nm. Here, we predict that the nanodomains with a wide size distribution are restricted to two characteristic sizes of the nanoheterogeneities inside the homogeneous glass. The complicated nanoscaled morphology was maintained up to $P_2$. Moreover, the conformational fractions became almost constant between 5.0 GPa and $P_2$. At $P_2$, the second glass–grass transition caused the disappearance of the prepeaks. Finally, homogeneous glass in $[C_8 mim][NO_3]$ was obtained above $P_2$. The heterogeneous glass–homogeneous glass transition at $P_2$ resembles the polyamorphism of water [2–4]. From the viewpoint of the cationic conforma-
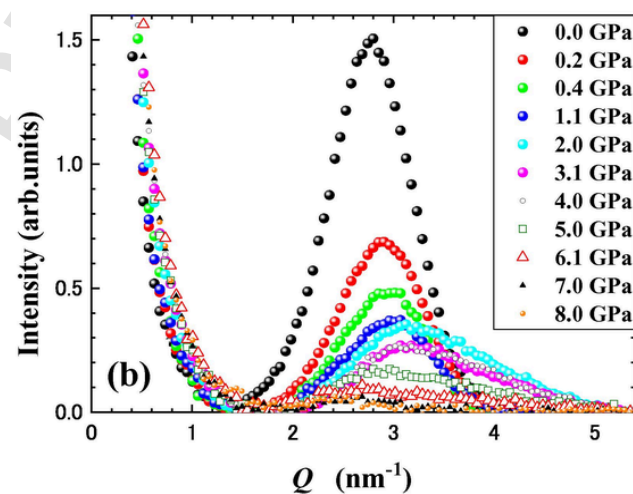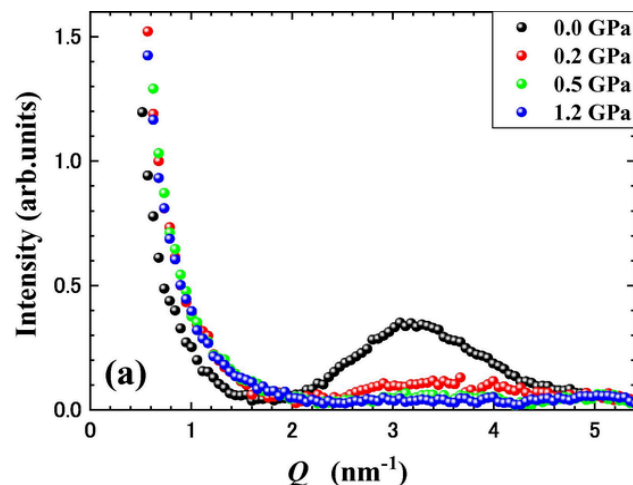


**Fig. 7.** Pressure-dependent SWAXS intensities of (a) $[C_6 mim][NO_3]$ and (b) $[C_8 mim][NO_3]$ at room temperature. SWAXS intensities were normalized to the Bragg intensity of the Kapton film.

tions, the *gauche* fraction increased again above $P_2$. The homogeneous glassy state could promote molecular packing efficiency using folding conformers.

## 4. Conclusions

Herein, HP-driven multiple-glass transitions of $[C_n mim][NO_3]$ ($n = 4, 6$, and 8) were clarified through Raman spectroscopy and SWAXS. $[C_4 mim][NO_3]$ exhibited a simple glass transition from homogeneous spL to homogeneous glass. The nanoheterogeneity of $[C_6 mim][NO_3]$ completely disappeared during spL. The HP glass of $[C_6 mim][NO_3]$ was homogeneous. A complicated triple-glass transition was observed in $[C_8 mim][NO_3]$. Even at $P_g$, nanoheterogeneity remained with decreasing prepeak intensity and prepeak broadening. Broad prepeak split close to $P_1$. The nanoheterogeneous double state was induced only in $[C_8 mim][NO_3]$. The two prepeaks vanished at $P_2$, and a homogeneous glassy state was formed. The heterogeneous glass–homogeneous glass transition of $[C_8 mim][NO_3]$ was similar to the polyamorphism of water. The alkyl chain length of the cations extensively influenced the HP-driven multiple-glass transitions of $[C_n mim][NO_3]$.

## CRediT authorship contribution statement

**Hiroshi Abe:** Writing – review & editing, Writing – original draft, Methodology, Investigation, Formal analysis, Data curation, Conceptualization. **Takaaki Hirano:** Data curation. **Hiroaki Kishimura:** Data curation. **Takahiro Takekiyo:** Methodology. **Yukihiro Yoshimura:** Supervision.

## Declaration of competing interest

The authors declare that they have no known competing financial interests or personal relationships that could have appeared to influence the work reported in this paper.

## Data availability

Data will be made available on request.

## Acknowledgments

## References

[1] C.G. Salzmann, Advances in the experimental exploration of water's phase diagram, J. Chem. Phys. 150 (2019) 060901–060909.
[2] O. Mishima, L.D. Calvert, E. Whalley, An apparently first-order transition between two amorphous phases of ice indued by pressure, Nature 314 (1985) 76–78.
[3] O. Mishima, H.E. Stanley, The relationship between liquid, supercooled and glassy water, Nature 396 (1998) 329–335.
[4] P.H. Poole, F. Sciortino, U. Essmann, H.E. Stanley, Phase behaviour of metastable water, Nature 360 (1992) 324–328.
[5] P. Gallo, K. Amann-Winkel, C.A. Angell, M.A. Anisimov, F. Caupin, C. Chakravarty, E. Lascaris, T. Loerting, A.Z. Panagiotopoulos, J. Russo, J.A. Sellberg, H.E. Stanley, H. Tanaka, C. Vega, L. Xu, L.G.M. Pettersson, Water: A Tale of Two Liquids, Chem. Rev. 116 (2016) 7463–7500.
[6] T.A. Kesselring, G. Franzese, S.V. Buldyrev, H.J. Herrmann, H.E. Stanley, Nanoscale Dynamics of Phase Flipping in Water near its Hypothesized Liquid-Liquid Critical Point, Sci. Rep. 2 (2012) 474–476.
[7] O. Mishima, T. Sumita, Equation of State of Liquid Water Written by Simple Experimental Polynomials and the Liquid-Liquid Critical Point, J. Phys. Chem. B 127 (2023) 1414–1421.
[8] K. Amann-Winkel, K.H. Kim, N.s Giovambattista, M. Ladd-Parada, A. Späh, F. Perakis, H. Pathak, C. Yang, T. Eklund, T.J. Lane, S. You, S. Jeong, J.H. Lee, I. Eom, M. Kim, J. Park, S.H. Chun, P.H. Poole, A. Nilsson, Liquid-liquid phase separation in supercooled water from ultrafast heating of low-density amorphous ice, Nature Commun. 14 (2023) 442–448.
[9] H. Tanaka, Liquid–liquid transition and polyamorphism, J. Chem. Phys. 153 (2020) 130901–130943.
[10] H. Ohno, M. Yoshizawa-Fujita, Y. Kohno, Functional Design of Ionic Liquids: Unprecedented Liquids that Contribute to Energy Technology, Bioscience, and Materials Sciences, Bull. Chem. Soc. Jpn. 92 (2019) 852–868.
[11] J. Kadokawa, Application of ionic liquids for the functional materialization of chitin, Mater. Adv. 3 (2022) 3355–3364.
[12] Y. Pei, Y. Zhang, J. Ma, M. Fan, S. Zhang, J. Wang, Ionic liquids for advanced materials, Mater. Today, Nano 17 (2022) 100159.
[13] J.N.A. Canongia Lopes, A.A.H. Pádua, Nanostructural Organization in Ionic Liquids, J. Phys. Chem. B 110 (2006) 3330–3335.
[14] A. Triolo, O. Russina, H.-J. Bleif, E. Di Cola, Nanoscale Segregation in Room Temperature Ionic Liquids, J. Phys. Chem. B 111 (2007) 4641–4644.
[15] H. Abe, H. Kishimura, Multistep phase transition in 1-decyl-3-methylimidazolium nitrate ionic liquid, J. Mol. Liq. 352 (2022) 118695–118698.
[16] H. Abe, T. Takekiyo, Y. Yoshimura, N. Hamaya, S. Ozawa, Crystal Polymorphs and Multiple Crystallization Pathways of Highly Pressurized 1-Ethyl-3-Methylimidazolium Nitrate, Aust. J. Chem. 72 (2019) 87–92.
[17] H. Abe, T. Takekiyo, Y. Yoshimura, K. Saihara, A. Shimizu, Anomalous Freezing of Nano-Confined Water in Room-Temperature Ionic Liquid 1-Butyl-3-Methylimidazolium Nitrate, ChemPhysChem 17 (2016) 1136–1142.
[18] T. Endo, T. Higuchi, Y. Kimura, DFT Study on Conformation of 1-Alkyl-3-methylimidazolium with Ethyl, Propyl, Butyl, Pentyl, and Hexyl Group, Bull. Chem. Soc. Jpn. 93 (2020) 720–729.
[19] H. Abe, Y. Yoshiichi, H. Kishimura, H. Sagayama, Low-temperature and high-pressure phase transitions in 1-decyl-3-methylimidazolium nitrate ionic liquid, Chem. Phys. Lett. 827 (2023) 140685–140687.
[20] H. Abe, H. Kishimura, M. Uruichi, Quasi-equilibrium phase transition in ionic liquid: 1-Decyl-3-methylimidazolium nitrate, submitted to J. Therm. Anal. Calorim.
[21] W. Cao, Y. Wang, G. Saielli, Metastable State during Melting and Solid–Solid Phase Transition of [CnMim][NO3] (n = 4–12) Ionic Liquids by Molecular Dynamics Simulation, J. Phys. Chem. B 122 (2018) 229–239.
[22] W. Cao, Y. Wang, Phase Behaviors of Ionic Liquids Heating from Different Crystal Polymorphs toward the Same Smectic-A Ionic Liquid Crystal by Molecular Dynamics Simulation, Crystals 9 (2019) 26.
[23] S. Li, Y. Wang, Percolation Phase Transition from Ionic Liquids to Ionic Liquid Crystals, Sci. Rep. 9 (2019) 13169.
[24] Y. Wang, W. Jiang, G.A. Voth, Spatial Heterogeneity in Ionic Liquids, in: Ionic Liquids IV, 975, American Chemical Society, 2007, pp. 272–307.
[25] Y. Yoshimura, H. Abe, T. Takekiyo, M. Shigemi, N. Hamaya, R.I. Wada, M. Kato, Superpressing of a Room Temperature Ionic Liquid, 1-Ethyl-3-methylimidazolium Tetrafluoroborate, J. Phys. Chem. B 117 (2013) 12296–12302.
[26] M.C.C. Ribeiro, A.A.H. Pádua, M.F. Costa Gomes, Glass transition of ionic liquids under high pressure, J. Chem. Phys. 140 (2014) 244514–244516.
[27] Y. Yoshimura, M. Shigemi, M. Takaku, M. Yamamura, T. Takekiyo, H. Abe, N. Hamaya, D. Wakabayashi, K. Nishida, N. Funamori, T. Sato, T. Kikegawa, Stability of the Liquid State of Imidazolium-Based Ionic Liquids under High Pressure at Room Temperature, J. Phys. Chem. B 119 (2015) 8146–8153.
[28] Y. Yoshimura, T. Takekiyo, Y. Koyama, M. Takaku, M. Yamamura, N. Kikuchi, D. Wakabayashi, N. Funamori, K. Matsuishi, H. Abe, N. Hamaya, High-pressure glass formation of a series of 1-alkyl-3-methylimidazolium bis(trifluoromethanesulfonyl) imide homologues, Phys. Chem. Chem. Phys. 20 (2018) 199–205.
[29] E. Patyk-Kaźmierczak, M. Kaźmierczak, A new high-pressure benzocaine polymorph — towards understanding the molecular aggregation in crystals of an important active pharmaceutical ingredient (API), Acta Cryst. B 76 (2020) 56–64.
[30] O. Shimomura, K. Takemura, H. Fujihisa, Y. Fujii, Y. Ohishi, T. Kikegawa, Y. Amemiya, T. Matsushita, Application of an imaging plate to high-pressure x-ray study with a diamond anvil cell, Rev. Sci. Instrum. 63 (1992) 967–973.
[31] K.H. Lee, U. Schnupf, B.G. Sumpter, S. Irle, Performance of Density-Functional Tight-Binding in Comparison to Ab Initio and First-Principles Methods for Isomer Geometries and Energies of Glucose Epimers in Vacuo and Solution, ACS Omega 3 (2018) 16899–16915.
[32] M.W. Schmidt, K.K. Baldridge, J.A. Boatz, S.T. Elbert, M.S. Gordon, J.H. Jensen, S. Koseki, N. Matsunaga, K.A. Nguyen, S. Su, T.L. Windus, M. Dupuis, J.A. Montgomery Jr, General atomic and molecular electronic structure system, J. Comput. Chem. 14 (1993) 1347–1363.
[33] S. Bilgili, F. Bardak, E. Kose, A. Atac, Investigation of the interionic interactions and spectroscopic features of 1-Octyl-3-methylimidazolium chloride, tetrafluoroborate, and hexafluorophosphate ionic liquids: An experimental survey and DFT modeling, J. Mol. Str. 1261 (2022) 132912–132914.
[34] G.J. Piermarini, S. Block, J.D. Barnett, Hydrostatic limits in liquids and solids to 100 kbar, J. Appl. Phys. 44 (1973) 5377–5382.
[35] S. Spange, R. Lungwitz, A. Schade, Correlation of molecular structure and polarity of ionic liquids, J. Mol. Liq. 192 (2014) 137–143.
[36] P. Naert, K. Rabaey, C.V. Stevens, Ionic liquid ion exchange: exclusion from strong interactions condemns cations to the most weakly interacting anions and dictates reaction equilibrium, Green Chem. 20 (2018) 4277–4286.
[37] K. Fujii, Y. Soejima, Y. Kyoshoin, S. Fukuda, R. Kanzaki, Y. Umebayashi, T. Yamaguchi, S. Ishiguro, T. Takamuku, Liquid Structure of Room-Temperature Ionic Liquid, 1-Ethyl-3-methylimidazolium Bis-(trifluoromethanesulfonyl) Imide, J. Phys. Chem. B 112 (2008) 4329–4336.
[38] K. Shimizu, C.E.S. Bernardes, J.N. Canongia Lopes, Structure and Aggregation in the 1-Alkyl-3-Methylimidazolium Bis(trifluoromethylsulfonyl)imide Ionic Liquid Homologous Series, J. Phys. Chem. B 118 (2014) 567–576.
[39] L.F.O. Faria, T.A. Lima, M.C.C. Ribeiro, Phase Transitions of the Ionic Liquid [C2C1im][NTf2] under High Pressure: A Synchrotron X-ray Diffraction and Raman Microscopy Study, Cryst. Growth Des. 17 (2017) 5384–5392.
[40] H. Abe, H. Kishimura, M. Uruichi, A phase variety of fluorinated ionic liquids: Molecular conformational and crystal polymorph, Spectrochim. Acta A 286 (2023) 121948.